

Improve thermoelectric properties of graphene nanoribbons based on resonant structure engineering

Yu-Xuan Kang(康宇轩), Shi-Yun Xiong(熊世云), and Hong-Liang Yi(易红亮)

Citation: Chin. Phys. B, 2026, 35 (**3**): 037301. DOI: 10.1088/1674-1056/ae1950
http://cpb.iphy.ac.cn; http://iopscience.iop.org/cpb

What follows is a list of articles you may be interested in

Enhanced thermoelectric properties of the topological phase of monolayer HfC

Wenlai Mu(母文来), Nisar Muhammad(穆罕默德·尼萨), Baojuan Dong(董宝娟), Nguyen Tuan Hung(阮俊兴), Huaihong Guo(郭怀红), Riichiro Saito(斋藤理一郎), Weijiang Gong(公卫江), Teng Yang(杨腾), and Zhidong Zhang(张志东)

Chin. Phys. B, 2025, 34 (**5**): 057301. DOI: 10.1088/1674-1056/adbd17

$GaInX_3$ (X = S, Se, Te): Ultra-low thermal conductivity and excellent thermoelectric performance

Zhi-Fu Duan(段志福), Chang-Hao Ding(丁长浩), Zhong-Ke Ding(丁中科), Wei-Hua Xiao(肖威华), Fang Xie(谢芳), Nan-Nan Luo(罗南南), Jiang Zeng(曾犟), Li-Ming Tang(唐黎明), and Ke-Qiu Chen(陈克求)

Chin. Phys. B, 2024, 33 (**8**): 087302. DOI: 10.1088/1674-1056/ad47e3

Optimization of thermoelectric properties in elemental tellurium via high pressure

Dongyao Zhao(赵东尧), Manman Yang(杨曼曼), Hairui Sun(孙海瑞), Xin Chen(陈欣), Yongsheng Zhang(张永胜), and Xiaobing Liu(刘晓兵)

Chin. Phys. B, 2023, 32 (**10**): 107305. DOI: 10.1088/1674-1056/ace15e

Strong anharmonicity-assisted low lattice thermal conductivities and high thermoelectric performance in double-anion Mo_2AB_2 (A = S, Se, Te; B=Cl, Br, I) semiconductors

Haijun Liao(廖海俊), Le Huang(黄乐), Xing Xie(谢兴), Huafeng Dong(董华锋), Fugen Wu(吴福根), Zhipeng Sun(孙志鹏), and Jingbo Li(李京波)

Chin. Phys. B, 2023, 32 (**10**): 107304. DOI: 10.1088/1674-1056/ace314

Facile fabrication of highly flexible, porous PEDOT: PSS/SWCNTs films for thermoelectric applications

Fu-Wei Liu(刘福伟), Fei Zhong(钟飞), Shi-Chao Wang(王世超), Wen-He Xie(谢文合), Xue Chen(陈雪), Ya-Ge Hu(胡亚歌), Yu-Ying Ge(葛钰莹), Yuan Gao(郜源), Lei Wang(王雷), and Zi-Qi Liang(梁子骐)

Chin. Phys. B, 2022, 31 (**2**): 027303. DOI: 10.1088/1674-1056/ac3502

SPECIAL TOPIC — Heat conduction and its related interdisciplinary areas

Improve thermoelectric properties of graphene nanoribbons based on resonant structure engineering

Yu-Xuan Kang(康宇轩)[1,2], Shi-Yun Xiong(熊世云)[3,†], and Hong-Liang Yi(易红亮)[1,2,‡]

[1] *School of Energy Science and Engineering, Harbin Institute of Technology, Harbin* 150001, *China*

[2] *Key Laboratory of Aerospace Thermophysics, Ministry of Industry and Information Technology, Harbin* 150001, *China*

[3] *Guangzhou Key Laboratory of Low-Dimensional Materials and Energy Storage Devices, School of Materials and Energy, Guangdong University of Technology, Guangzhou* 510006, *China*

(Received 14 August 2025; revised manuscript received 23 October 2025; accepted manuscript online 30 October 2025)

Resonant graphene nanoribbons (GNRs), consisting of GNRs with engineered resonant side structures, offer a promising route to suppress low-frequency phonon transport and significantly reduce lattice thermal conductivity, thereby enhancing thermoelectric performance. In this work, we investigate the thermoelectric properties of resonant GNRs using molecular dynamics simulations combined with the linear-scaling quantum transport (LSQT) method, explicitly accounting for electron–phonon coupling. Our results indicate that while resonance structures moderately degrade the electrical conductivity and Seebeck coefficient, they dramatically reduce the lattice thermal conductivity, which far outweighs the electronic transport losses and leads to an overall improvement in thermoelectric performance. By optimizing the key geometric parameters of the resonant structures — height (H_{Re}) and period (L_{p}) — we achieve a peak ZT of 0.135 at $H_{\mathrm{Re}} = 1.5$ nm and $L_{\mathrm{p}} = 7$ nm, representing a threefold enhancement over pristine GNRs. This improvement stems from the decoupling of phonon and electron transport, enabled by resonant phonon localization. Our findings not only elucidate the role of resonant structures in tuning thermoelectric properties but also provide a general strategy for designing high-performance low-dimensional thermoelectric materials through targeted phonon engineering.

Keywords: thermoelectric properties, graphene nanoribbons, resonant structure, thermal conductivity

PACS: 73.50.Lw, 74.25.fc, 73.63.–b, 81.05.U–

DOI: 10.1088/1674-1056/ae1950 **CSTR:** 32038.14.CPB.ae1950

1. Introduction

Since its discovery in 2004, graphene has attracted extensive interest due to its distinctive geometric structure, excellent mechanical properties,[1] remarkable thermal stability,[2] exceptional optical characteristics,[3,4] and ultra-high carrier mobility.[5] Graphene nanoribbons (GNRs), which are quasi-one-dimensional derivatives of graphene, exhibit a tunable bandgap, excellent electrical properties, and adjustable thermal conductivity, making them promising candidates for thermoelectric applications.[5–7] The thermoelectric efficiency of a material is quantified by the dimensionless figure of merit,[8,9] $ZT = T\sigma S^2/\kappa$, where S is the Seebeck coefficient, σ is the electrical conductivity, and κ is the total thermal conductivity (comprising electron κ_{el} and phonon κ_{ph} contributions), and T is the absolute temperature. Despite GNRs exhibiting lower thermal conductivity than pristine graphene, their ZT values remain modest (typically ≤ 0.01) due to the still-high thermal conductivity.[10] Therefore, optimizing the thermoelectric performance of GNRs — by enhancing S and σ while suppressing κ — is a crucial challenge.

The thermoelectric properties of GNRs can be effectively modulated through structural modifications, including width,[11,12] edge roughness,[11,13] defects,[14,15] doping[16,17] and resonant structures.[18] Among these, resonant structures (e.g., side branches) are particularly promising because they are capable of suppressing low-frequency phonon transport, allowing synergistic engineering with other scattering mechanisms (e.g., point defects) to reduce κ_{ph} across the entire phonon spectrum.[18,19] Such resonant phonon localization has been demonstrated to drastically reduce κ in silicon nanowires,[19–22] silicon thin films[23–25] and GNRs,[26,27] primarily attributed to hybrid coupling between resonant phonons and low-frequency propagating modes. For instance, in MoS_2 nanoribbons with side branches, the phonon thermal conductance of the nanoribbon is reduced from 0.51 nW/K to 0.09 nW/K, elevating ZT from 0.72 to 1.93.[28] The ZT value of graphenylene nanoribbons is improved from 0.5 to 1.8 by introducing side branches.[29] Resonant side branches in poly-butadiene-cyclooctatetraene-framework carbon allotrope (PBCF-graphene) GNRs (A-PBCF-GNRs) significantly improve ZT, attributed to the remarkable reduction in thermal conductivity of branched A-PBCF-GNRs caused by the localized electronic and phonon states.[30] Experimentally,

†Corresponding author. E-mail: syxiong@gdut.edu.cn

‡Corresponding author. E-mail: yihongliang@hit.edu.cn

© 2026 Chinese Physical Society and IOP Publishing Ltd. All rights, including for text and data mining, AI training, and similar technologies, are reserved.

Spann *et al.* demonstrated decoupled control of lattice thermal conductivity from the Seebeck coefficient and electrical conductivity in GaN-nanopillar-decorated silicon membranes, highlighting the potential of resonant structures for *ZT* enhancement.[31]

While the impact of resonant structures on phonon transport has been studied systematically, covering size effects,[19] distribution patterns,[32] resonant coupling mechanisms,[27,33] and synergistic effects with other scattering sources,[34,35] their impact on electron transport remains less explored. The understanding of electron transport in resonant structures is still incomplete. Prior theoretical studies often relied on ballistic transport models (e.g., non-equilibrium Green's function, NEGF) that neglect electron–phonon coupling, limiting their applicability to short-channel systems.

In this work, we combine molecular dynamics simulations with the linear-scaling quantum transport (LSQT) method[36] to investigate the thermoelectric properties of GNRs with resonant side branches, explicitly accounting for electron–phonon interactions through molecular dynamics trajectories. By regulating the height and periodicity of the resonant structures, we demonstrate precise control over thermoelectric transport and achieve a significant enhancement in *ZT*.

2. Model and method

2.1. Model

The resonant GNRs consist of a pristine GNR decorated with resonant structures on both edges, as illustrated in Fig. 1. In our simulations, the width of the resonant branches W_{Re} and the width of the main GNR were fixed at 3 nm and 5 nm, respectively, while the period of the whole structure L_{p} and the height of the side branches H_{Re} were systematically varied to investigate their influence on thermoelectric transport. Such resonant GNR structures have been experimentally fabricated with atomic precision via bottom-up synthesis.[37] We keep H_{Re} smaller than W_{Re} to ensure stable dynamics of the whole structure.

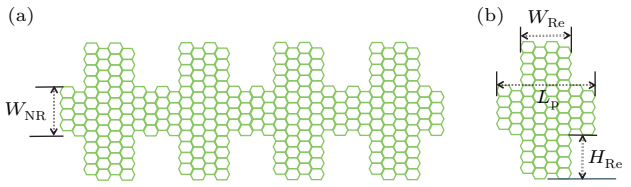


Fig. 1. (a) Schematic illustration of the resonant GNR structure. (b) Minimal repeating unit showing the key geometric parameters: nanoribbon width W_{NR}, resonator period L_{p}, height H_{Re}, and width W_{Re}.

2.2. Method

The total thermal conductivity comprises contributions from both electrons and phonons. Here, κ_{ph} is calculated using the homogeneous non-equilibrium molecular dynamics (HNEMD) method.[38] This approach is physically equivalent to equilibrium molecular dynamics (EMD)[39] but is computationally more efficient. In this method, an external driving force is applied to each atom to induce heat flow and is given by

$$\boldsymbol{F}_i^{\mathrm{ext}} = E_i \boldsymbol{F}_e + \boldsymbol{F}_e \cdot \boldsymbol{W}_i, \tag{1}$$

where $\boldsymbol{W}_i$ is the per-atom virial tensor for atom i

$$\boldsymbol{W}_i = \sum_{j \neq i} \frac{\partial U_j}{\partial \boldsymbol{r}_{ij}} \otimes \boldsymbol{r}_{ij}. \tag{2}$$

Here, U_j is the potential energy of particle j, and $\boldsymbol{r}_{ij} = \boldsymbol{r}_j - \boldsymbol{r}_i$, with $\boldsymbol{r}_i$ and $\boldsymbol{r}_j$ being the positions of particles i and j, respectively. The lattice thermal conductivity tensor is then calculated as

$$\frac{\langle J^{\alpha} \rangle}{TV} = \sum_{\beta} \kappa_{\mathrm{ph}}^{\alpha\beta} F_e^{\beta}, \tag{3}$$

where T is the system temperature, V is the system volume, and $\langle \cdot \rangle$ denotes the ensemble average of the heat current.[40]

To model electron transport properties, we integrate molecular dynamics (MD) simulations with the linear-scaling quantum transport (LSQT) method.[41] The MD simulation treats the motion of atomic nuclei classically using Newton's equations. For each ionic snapshot generated by MD, we perform a fully quantum mechanical calculation using the LSQT method. Unlike conventional NEGF methods, this framework explicitly incorporates electron–phonon coupling by leveraging MD trajectories, while its linear scalability with system size enables efficient simulations of large-scale, structurally complex systems.[42] Within the LSQT framework, the electronic Hamiltonian is constructed using a bond-length-dependent tight-binding (TB) model, where bond parameters are dynamically updated based on MD-derived atomic configurations. This method captures electron–phonon coupling effects by concurrently simulating electronic and ionic time evolution, allowing quantitative evaluation of the impact of phonon scattering and structural disorder on charge transport. It has been demonstrated that this method can reproduce the experimentally measured electrical conductivity of graphene,[36,43] demonstrating the accuracy of the approach.

The LSQT method computes the time-dependent electrical conductivity, $\Sigma(E,t)$, via two methodologies: the velocity autocorrelation (VAC) function and the mean squared displacement (MSD) approach. In this work, we adopt the VAC formalism, where the energy E- and correlation time t-dependent electrical conductivity $\Sigma(E,t)$ is obtained[42]

$$\Sigma(E,t) = \frac{2e^2}{\Omega} \int_0^t \mathrm{Tr}\left(\delta\left(E-H\right) \mathrm{Re}\left(\hat{V}\hat{V}\left(\tau\right)\right)\right) \mathrm{d}\tau, \tag{4}$$

where e is the elementary charge, Ω is the system volume, $\delta\left(E-\hat{H}\right)$ is the energy resolution operator, $\hat{V}$ is the velocity operator, and $\hat{V}\left(\tau\right) = \mathrm{e}^{\mathrm{i}\hat{H}\tau}\hat{V}\,\mathrm{e}^{-\mathrm{i}\hat{H}\tau}$ is the time-evolution velocity operator, with $\hat{H}$ being the electron Hamiltonian.

The semi-classical conductivity $\Sigma(E)$ is obtained by time-averaging $\Sigma(E,t)$ after convergence

$$\Sigma(E) = \frac{1}{t_2 - t_1} \int_{t_1}^{t_2} \Sigma(E,t)\,\mathrm{d}t. \tag{5}$$

This quantity represents the transport distribution function (TDF), which serves as the foundation for thermoelectric property calculations.[44–49] The electron transport properties as a function of chemical potential at temperature T are defined based on the following functional integrals ($n = 0,1,2$)

$$X_n(\mu,T) = \int -\frac{\partial f(E,\mu,T)}{\partial E} E^n \Sigma(E)\,\mathrm{d}E, \tag{6}$$

where $f(E,\mu,T)$ is the Fermi–Dirac distribution.

The electrical conductivity $\sigma(\mu,T)$, Seebeck coefficient $S(\mu,T)$, and electronic thermal conductivity $\kappa_{\mathrm{el}}(\mu,T)$ are then obtained as

$$\sigma(\mu,T) = X_0(\mu,T), \tag{7}$$

$$S(\mu,T) = -\frac{1}{eT}\left(\frac{X_1(\mu,T)}{X_0(\mu,T)} - \mu\right), \tag{8}$$

$$\kappa_{\mathrm{el}}(\mu,T) = \frac{1}{e^2 T}\left(X_2(\mu,T) - \frac{X_1^2(\mu,T)}{X_0^2(\mu,T)}\right). \tag{9}$$

Finally, the dimensionless thermoelectric figure of merit ZT is calculated by combining these results with the phonon thermal conductivity obtained from HNEMD

$$ZT(\mu,T) = \frac{S^2(\mu,T)\,\sigma(\mu,T)}{\kappa_{\mathrm{ph}} + \kappa_{\mathrm{el}}(\mu,T)} T. \tag{10}$$

All computational workflows for electronic and thermal transport properties in this work were performed using the GPUMD (Graphics Processing Unit Molecular Dynamics) package.[50] In MD simulations, all interatomic interactions were modeled using a neuroevolution potential (NEP)[51] specifically developed for carbon systems.[43] The NEP provides accurate interatomic forces at the quantum mechanical level while remaining computationally efficient enough for large-scale molecular dynamics simulations. As a result, it can correctly describe atomic trajectories, which are essential for modeling subtle electronic redistribution in resonant structures. For lattice thermal conductivity calculations using the HNEMD method, systems were first equilibrated under the NVT ensemble for 100 ps to achieve full structural relaxation. The time step was chosen to be 1 fs, which is sufficiently small to ensure energy conservation during simulations. A carefully calibrated dimensionless driving force of 0.0001 was applied to each atom, ensuring operation within the linear response regime while maintaining an optimal signal-to-noise ratio. We employed a simulation cell of 50 nm length with periodic boundary conditions in the transport direction and aperiodic boundaries in the other directions. Each simulation ran for 4 ns to guarantee proper convergence of the thermal conductivity values. To ensure statistical reliability, lattice thermal conductivity was obtained by averaging results from three independent simulations.

In the electron transport calculations using the LSQT method, atomic trajectories were obtained from MD simulations for structures 5000 nm long, with periodic boundary conditions applied along the transport axis. The electronic Hamiltonian was constructed at each time step based on instantaneous atomic configurations. The electron transport properties were calculated over 1000 steps to ensure convergence, with final values averaged across three independent calculations to minimize statistical fluctuations.

3. Results and discussion

3.1. Pristine graphene nanoribbons with varying widths

We first investigated the electronic transport properties of pristine graphene nanoribbons with varying widths. Armchair-edged graphene nanoribbons (AGNRs) were selected to systematically study the width-dependent thermoelectric performance, with a system length of 5000 nm to eliminate size effects. Figure 2(a) presents the density of states (DOS) for AGNRs of varying widths ($W_{\mathrm{NR}} = 2$ nm, 5 nm, and 10 nm). Narrow AGNRs ($W_{\mathrm{NR}} = 2$ nm) exhibit prominent van Hove singularities in their DOS, characteristic of one-dimensional quantum confinement. As the width increases to 10 nm, these singularities progressively diminish, with the DOS converging toward the characteristic profile of two-dimensional graphene. This evolution reflects a dimensional crossover from one-dimensional to quasi-two-dimensional electronic behavior as the system width increases. According to the DOS, a significant bandgap of 0.7 eV is observed for 2 nm-wide AGNRs, which is in good agreement with literature values.[52] This bandgap decreases dramatically to 0.26 eV at $W_{\mathrm{NR}} = 5$ nm and ultimately vanishes at $W_{\mathrm{NR}} = 10$ nm. This systematic reduction in bandgap with increasing width has important implications for thermoelectric transport properties.

We next examined the width dependence of key thermoelectric transport parameters, i.e., the electrical conductivity (σ), electronic thermal conductivity (κ_{el}), and Seebeck coefficient (S). The electrical conductivity near the Fermi level ($\mu = 0$) shows a progressive increase with AGNR width (Fig. 2(b)). This trend directly results from the narrowing bandgap, which significantly reduces the energy barrier for electron excitation from the valence to the conduction band. The electronic thermal conductivity (Fig. 2(c)) exhibits a similar energy dependence to σ, obeying the Wiedemann–Franz relation as expected for electronic transport. The Seebeck coefficient demonstrates an inverse correlation with σ across all widths (Fig. 2(d)). This relation arises because while σ de-

pends strongly on carrier concentration, increasing carrier concentration leads to a corresponding decrease in S. Therefore, the maximum S values observed near the Fermi level in AGNRs decrease with increasing ribbon width. This fundamental trade-off between σ and S presents an important challenge for optimizing thermoelectric performance in nanoribbon systems.

Our investigation of phonon transport reveals significant width-dependent behavior in the thermal conductivity of AGNRs. As shown in Fig. 3(a), the phonon thermal conductivity (κ_{ph}) decreases systematically from 797.3 $W{\cdot}m^{-1}{\cdot}K^{-1}$ for 10 nm-wide ribbons to 572.3 $W{\cdot}m^{-1}{\cdot}K^{-1}$ for 2 nm-wide ribbons. This substantial reduction arises primarily from enhanced phonon–boundary scattering in narrower ribbons, where the increased proportion of edge atoms introduces additional scattering centers that effectively suppress phonon transport.

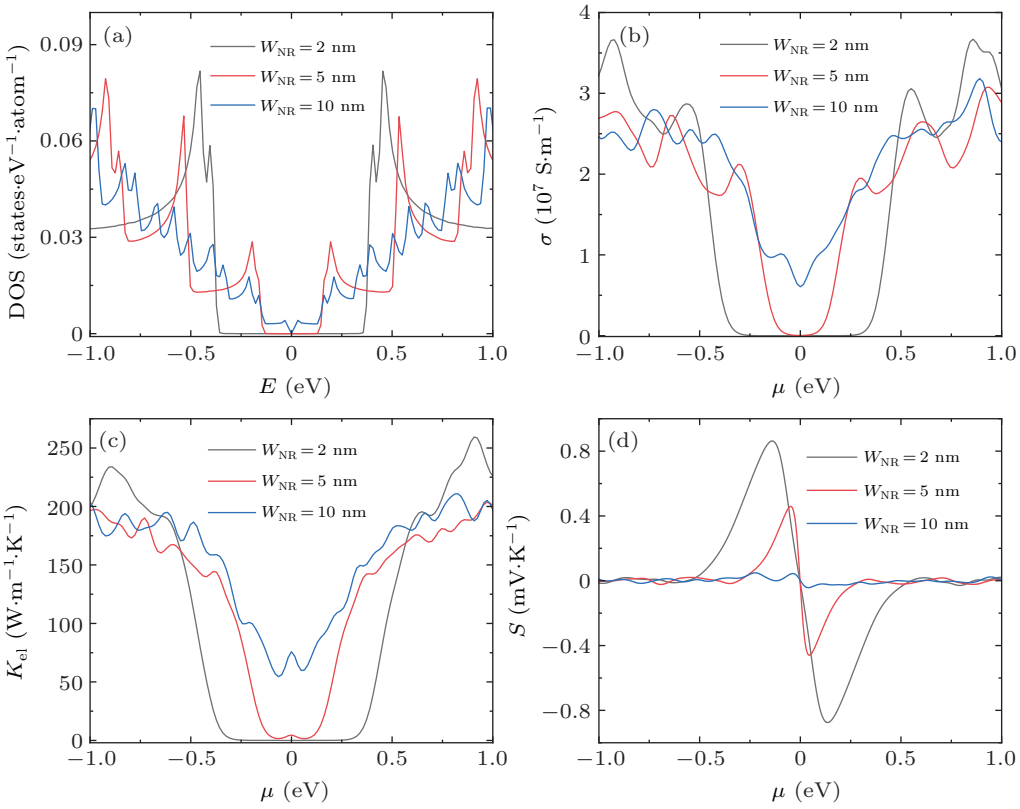


Fig. 2. Width-dependent electronic and thermoelectric properties of armchair GNRs. (a) DOS, (b) electrical conductivity (σ), (c) electronic thermal conductivity (κ_{el}), and (d) Seebeck coefficient (S) for AGNRs with widths of 2 nm, 5 nm, and 10 nm.

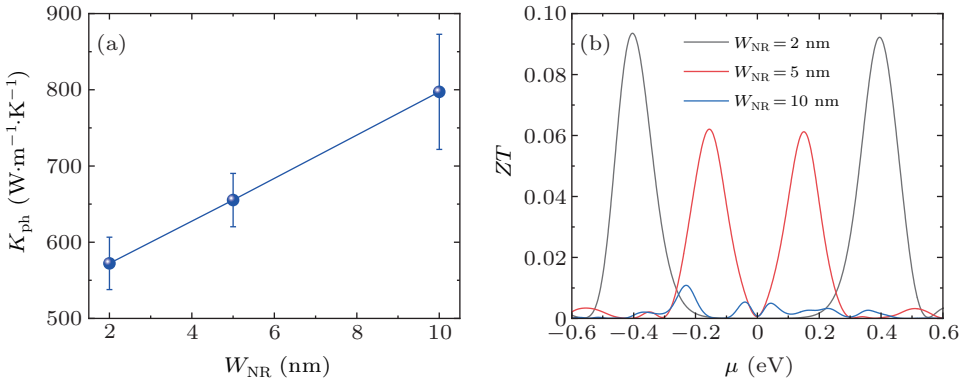


Fig. 3. (a) Variation of lattice thermal conductivity with the width of AGNRs. (b) Thermoelectric figure of merit ZT of AGNRs with different widths.

By combining these phonon transport results with our electronic transport properties, we calculated the thermoelectric figure of merit (ZT) using Eq. (10). Figure 3(b) shows that ZT exhibits characteristic peaks with varying chemical potential, representing the optimal ZT values achievable through either p-type or n-type doping. Notably, we observe a strong correlation between ribbon width and thermoelectric performance: the maximum ZT value increases gradually as the width decreases, from 0.005 for 10 nm-wide ribbons to 0.063 and 0.095 for 5 nm-wide and 2 nm-wide ribbons, respectively.

The chemical potentials corresponding to these maximum *ZT* values are also width dependent. For the 10 nm-wide ribbons, peak *ZT* occurs at a relatively low chemical potential of 0.055 eV, while the 2 nm-wide ribbons require a significantly higher 0.41 eV to reach their maximum *ZT*. This shift indicates that achieving optimal thermoelectric performance in narrower ribbons demands substantially higher doping concentrations. The width-dependent behavior of both *ZT* magnitude and optimal doping level provides crucial insights for designing graphene nanoribbon-based thermoelectric devices, particularly in balancing the trade-offs between dimensionality effects and doping requirements.

3.2. Graphene nanoribbons with resonant structures

Having established the baseline properties of pristine GNRs, we systematically investigated the effects of resonant structures by introducing side branches with $W_{\mathrm{Re}} = 3$ nm, $H_{\mathrm{Re}} = 1.5$ nm, and $L_{\mathrm{p}} = 6$ nm on 5 nm-wide GNRs. Figure 4 presents a comprehensive comparison of thermoelectric properties between pristine and resonant-modified structures at 300 K, revealing several key phenomena.

The introduction of resonant structures produces significant modifications to the electronic transport characteristics. As shown in Fig. 4(a), the TDF experiences notable suppression, leading to reduced σ compared to pristine GNRs (Fig. 4(b)). This effect stems from two primary mechanisms: the hybridization of resonant phonon modes with the host nanoribbon creates additional electron scattering channels, disrupting charge transport; and the electronic structure undergoes modification, exhibiting both bandgap widening and the emergence of impurity-like states within the band gap, as evidenced by small peaks in the TDF of resonant GNRs.

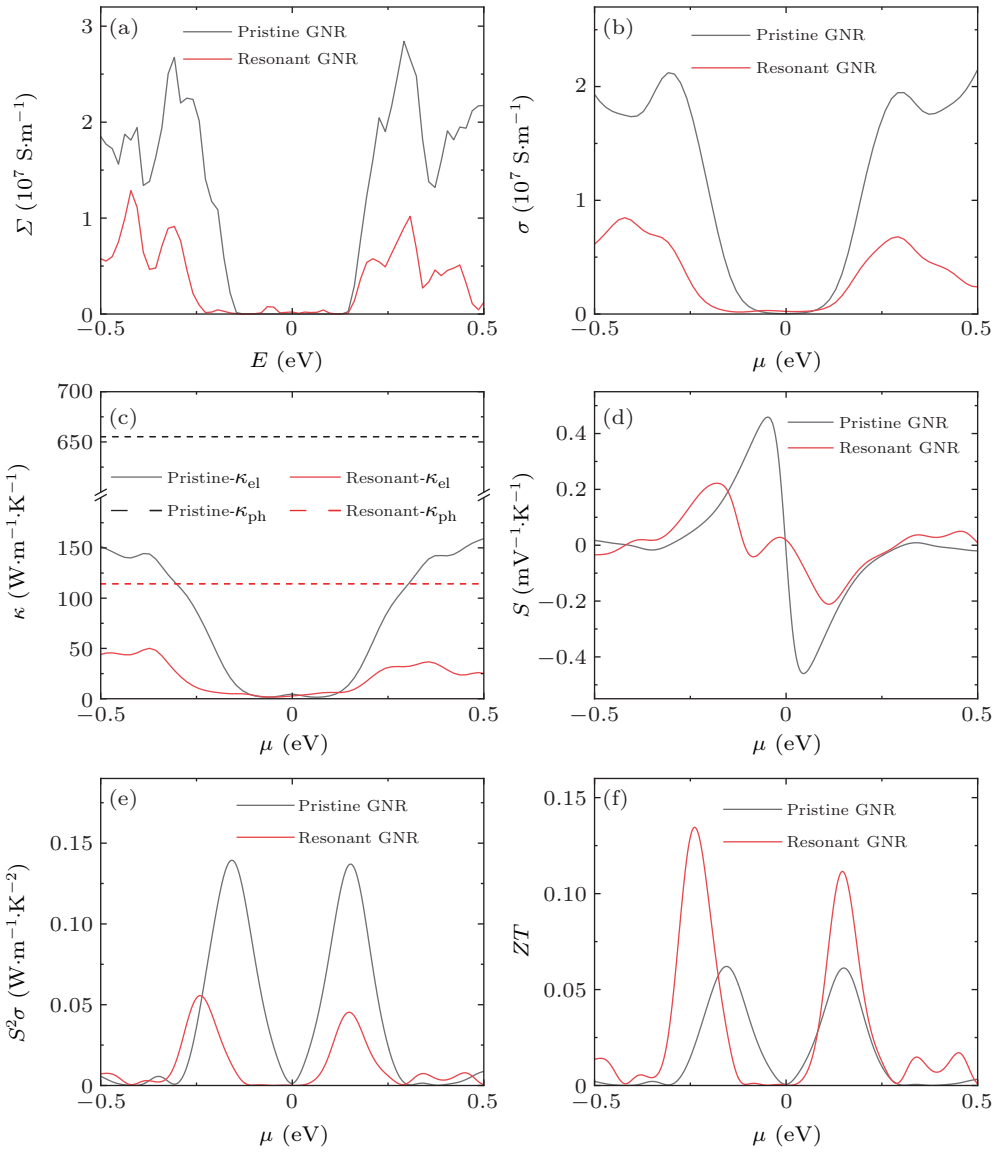


Fig. 4. Comparison of transport properties of pristine and resonant GNRs at 300 K. (a) transport distribution function (TDF), (b) electrical conductivity (σ), (c) electronic thermal conductivity (κ_{el}) and lattice thermal conductivity (κ_{ph}), (d) Seebeck coefficient (S), (e) power factor ($S^2\sigma$), and (f) thermoelectric figure of merit (ZT).

The thermal transport properties reveal particularly striking behavior. The electronic thermal conductivity decreases proportionally with electrical conductivity, consistent with the Wiedemann–Franz law.[53] More remarkably, the phonon thermal conductivity shows a six-fold reduction from 655.3 $W{\cdot}m^{-1}{\cdot}K^{-1}$ in pristine GNRs to 115 $W{\cdot}m^{-1}{\cdot}K^{-1}$ in resonant GNRs (Fig. 4(c)), which is in good agreement with literature values,[54] far exceeding the decrease in electrical conductivity. The introduction of resonant structures brings numerous flat bands in phonon dispersion. These flat resonant modes not only reduce the group velocity of the propagating modes inside the main GNR, but also decrease their relaxation time. This disproportionate suppression of phonon transport relative to electron transport proves crucial for thermoelectric enhancement. The Seebeck coefficient S exhibits more complex behavior: while generally reduced by the resonant structures, the degradation becomes less pronounced at higher chemical potentials. Notably, we observe an anomalous abrupt change in S at $\mu = -0.1$ eV (Fig. 4(d)), which is mainly related to the impurity-like states introduced within the bandgap.

The peak power factor (PF) shows the expected reduction from 0.135 $W{\cdot}m^{-1}{\cdot}K^{-1}$ in pristine GNRs to approximately 0.05 $W{\cdot}m^{-1}{\cdot}K^{-1}$ in resonant GNRs (Fig. 4(e)). However, despite this decrease, the peak thermoelectric figure of merit ZT demonstrates significant improvement — increasing from 0.065 in pristine GNRs to 0.12 (n-type) and 0.135 (p-type) in resonant GNRs (Fig. 4(f)). This counterintuitive result highlights the dominant role of phonon suppression in enhancing ZT, even when electronic transport properties are somewhat compromised.

To optimize these effects, we performed systematic variation of resonant structure dimensions H_{Re} and L_p while maintaining constant main ribbon width ($W_{NR} = 5$ nm) and side chain widths ($W_{Re} = 3$ nm). This analysis elucidates the impact of resonant structure parameters on thermoelectric properties, showcasing extremities in power factor and thermoelectric figure of merit.

Notably, the lattice thermal conductivity exhibits a strong dependence on resonant structure geometry, decreasing with increasing H_{Re} and decreasing L_p (Fig. 5(a)). For instance, at $H_{Re} = 1$ nm and $L_p = 10$ nm, the thermal conductivity measures 175 $W{\cdot}m^{-1}{\cdot}K^{-1}$, which is reduced to approximately 80 $W{\cdot}m^{-1}{\cdot}K^{-1}$ as H_{Re} increases to 3 nm and L_p decreases to 6 nm. This trend reflects enhanced hybridizations between resonant and propagating phonons. Increasing the height and decreasing the period of the resonant structure increases the density of resonant phonons, thereby enhancing the coupling between resonant and propagating modes and decreasing the thermal conductivity.[37,49] In addition, larger H_{Re} reduces the frequency of resonance modes, thus it is able to hinder phonon transport at much lower frequencies,[17] which exhibit large phonon mean free paths and contribute significantly to thermal conductivity. The PF exhibits a non-monotonic dependence on geometric parameters (Fig. 5(b)), reaching a global maximum at $H_{Re} = 1.5$ nm across all L_p values. The combined effects yield maximum ZT values when both phonon suppression and electronic transport are optimized. In general, ZT increases with decreasing L_p due to suppressed lattice thermal conductivity. Through careful resonant structure engineering, we achieve a peak ZT of 0.137, representing an order of magnitude enhancement over pristine GNRs and demonstrating the significant potential of this approach for thermoelectric applications. These results establish clear design principles for optimizing GNR-based thermoelectric materials through resonant structure engineering, where careful balancing of geometric parameters can selectively suppress phonon transport while maintaining reasonable electronic performance.

To systematically elucidate the structural parameter dependence of thermoelectric properties, we analyze the evolution of key transport coefficients with resonant structure periodicity (L_p) at the chemical potential corresponding to maximum ZT for resonant GNRs. Both electrical conductivity σ and electronic thermal conductivity κ_{el} decrease with increasing L_p (Figs. 6(a) and 6(b)). Notably, the Seebeck coefficient remains relatively unchanged across the tested periodicities. The combined periodicity-dependent σ and S drives a progressive decline in peak power factor (PF_{max}) with

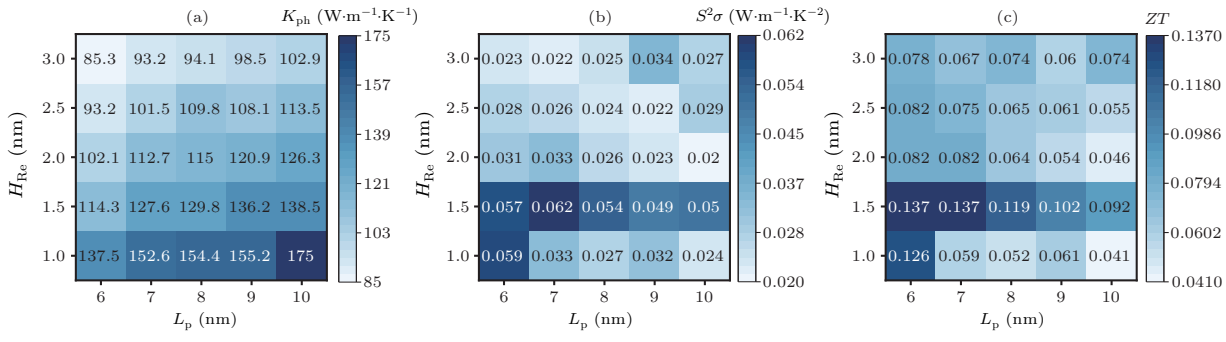


Fig. 5. Variation of thermoelectric properties with resonant structure height H_{Re} and period L_p at 300 K. (a) phonon thermal conductivity (κ_{ph}), (b) power factor ($S^2\sigma$), (c) thermoelectric figure of merit (ZT).

increasing L_p (Fig. 6(c)). Despite these electronic transport changes, phonon thermal conductivity remains dominant, exceeding electronic thermal conductivity by one order of magnitude. Consequently, ZT decreases with larger periods due to both reduced power factor and increased phonon thermal conductivity.

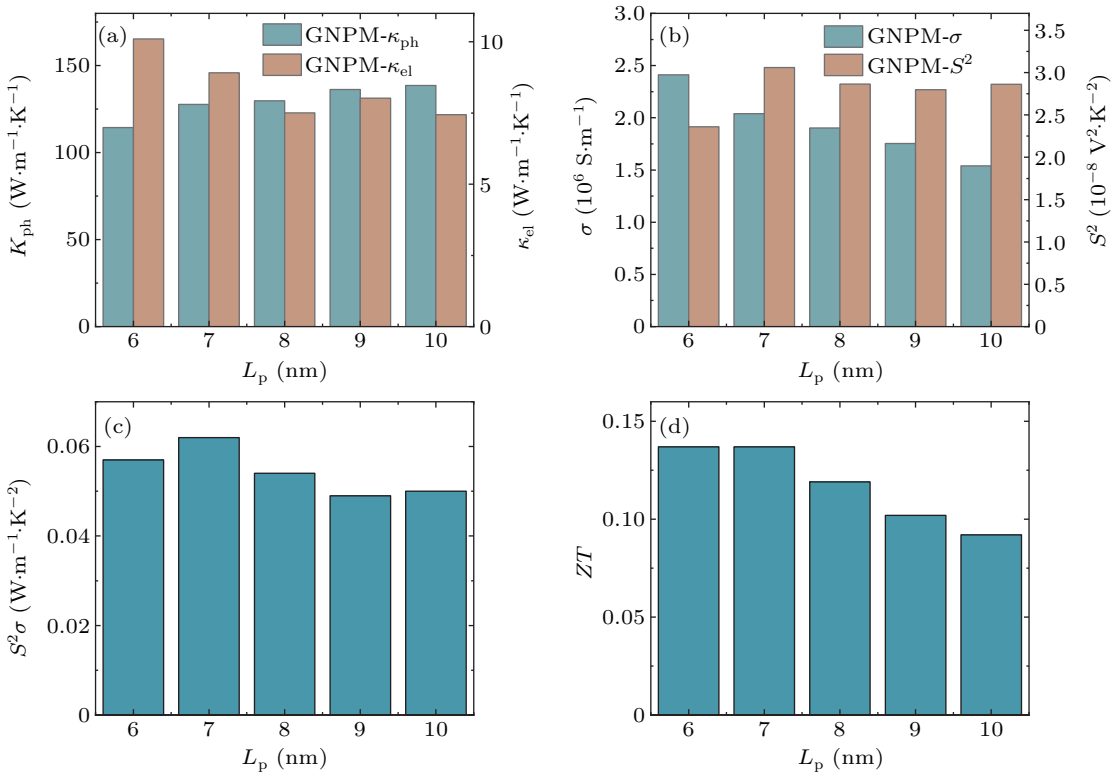


Fig. 6. Periodicity-dependent thermoelectric properties for resonant GNRs ($H_{Re} = 1.5$ nm). (a) lattice thermal conductivity (κ_{ph}) and electronic thermal conductivity (κ_{el}), (b) electrical conductivity (σ) and Seebeck coefficient (S), (c) power factor ($S^2\sigma$), and (d) thermoelectric figure of merit (ZT). All values are at the chemical potential corresponding to the peak ZT_{max}.

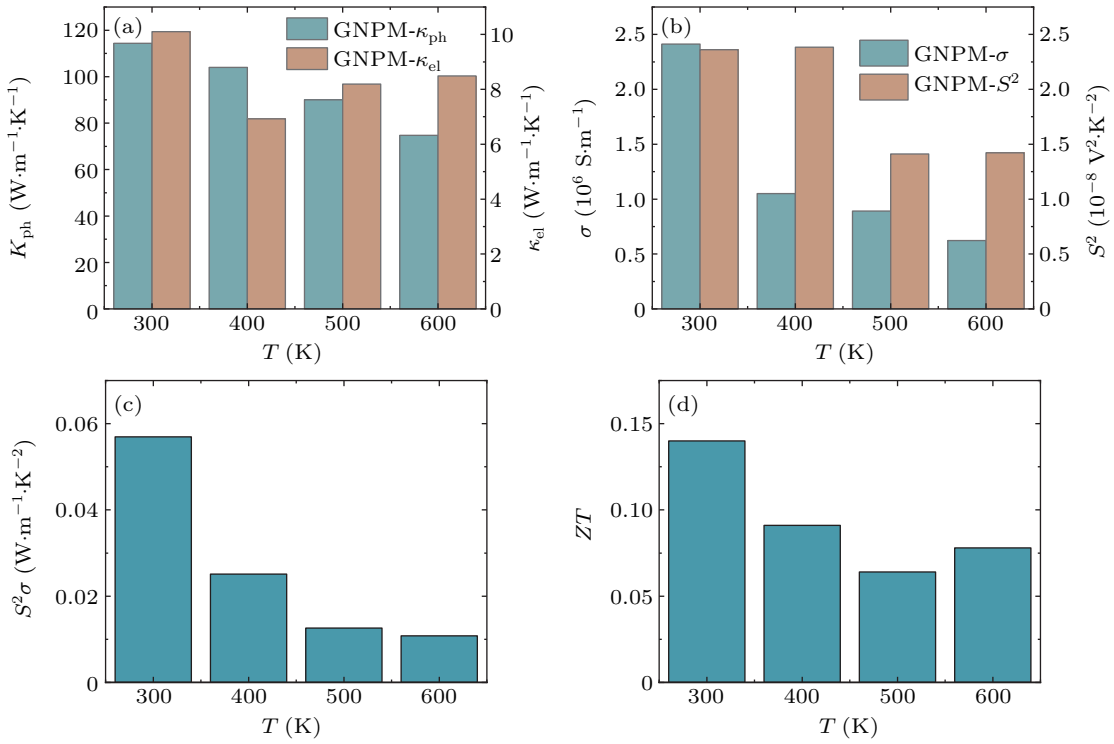


Fig. 7. Temperature evolution of thermoelectric properties for optimized resonant GNRs ($W_{NR} = 5$ nm, $H_{Re} = 1.5$ nm, $L_p = 6$ nm). (a) lattice thermal conductivity (κ_{ph}) and electronic thermal conductivity (κ_{el}), (b) electrical conductivity (σ) and Seebeck coefficient (S), (c) power factor ($S^2\sigma$), and (d) thermoelectric figure of merit (ZT). All values are at the chemical potential corresponding to the peak ZT_{max}.

The thermoelectric properties of resonant GNRs (W_{NR} = 5 nm, $H_{Re} = 1.5$ nm, and $L_p = 6$ nm) show strong temperature sensitivity between 300 K and 600 K (Fig. 7). κ_{ph} decreases monotonically with temperature (Fig. 7(a)) due to intensified phonon-phonon umklapp scattering. The elevated temperature also reduces σ due to enhanced electron–phonon scattering from amplified lattice vibrations (Fig. 7(b)). In contrast, κ_{el} exhibits non-monotonic behavior: it decreases until 400 K and then increases (Fig. 7(a)). This inconsistent variation of electrical conductivity and electronic thermal conductivity with temperature signifies the breakdown of the Wiedemann–Franz law, which will be analyzed later. The Seebeck coefficient undergoes an abrupt 21% reduction between 400–500 K (Fig. 7(b)), which may be attributed to the smearing effect of the Fermi–Dirac distribution. The *PF* declines progressively with temperature (Fig. 7(c)) due to simultaneous degradation of σ and S, indicating thermally degraded electronic transport properties. The competing effects between electronic and thermal transport properties produce distinct variations of *ZT* with temperature: it decreases below 500 K (electron-dominated), then increases above 500 K (phonon-dominated) (Fig. 7(d)).

3.3. The violation of Wiedemann–Franz law

The contrasting temperature trends of κ_{el} (Fig. 7(a)) and σ (Fig. 7(b)) in resonant GNRs reveal a fundamental violation of the Wiedemann–Franz (W–F) law, which relates σ, κ_{el}, and T through $\kappa_{el} = L\sigma T$. Here, the Lorenz number L is theoretically constant for degenerate electron gases, $L_0 = \frac{\pi^2 k_B^2}{3e^2} = 2.44 \times 10^{-8}\ \mathrm{W{\cdot}\Omega{\cdot}K^2}$. To illustrate the degree of deviation from the theoretical value, we calculated the actual Lorenz number $L = \kappa_{el}/(\sigma T)$ and further evaluated L/L_0 at different temperatures. The corresponding results are shown in Fig. 8. It is observed that L/L_0 increases from 0.55 at 300 K to 0.92 at 600 K, indicating gradual restoration of W–F compliance at higher temperatures in resonant GNRs. The violation of the W–F law stems from peaked features in the TDF (Fig. 4(a))[41,45] and the limited number of excited electrons at low temperatures in resonant GNRs. As temperature increases, more electrons become excited, driving L/L_0 toward unity,[55] as the W–F law is derived from the one-electron approximation and applies to Fermi liquid systems.[56] Additionally, as reported in previous studies,[41] asymmetric probability density distributions and larger bandgap formation also contribute to violations of the W–F law. This strong violation at low temperatures enables independent optimization of electronic and thermal transport, representing a key mechanism for achieving high *ZT* values in these nanostructured materials.

A comprehensive understanding of these geometric and thermal effects provides critical design principles for resonant-structure-based thermoelectric devices, particularly for balancing structural parameters with operational temperature ranges while exploiting unique electron–phonon decoupling opportunities.

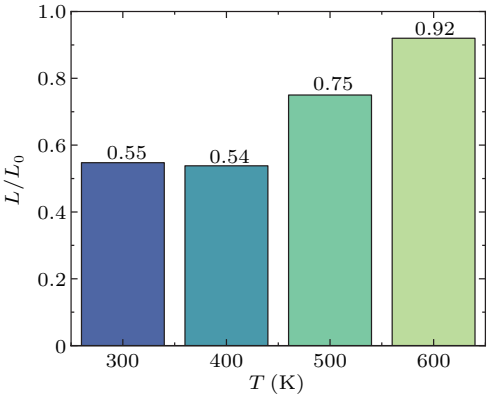


Fig. 8. Ratio of the calculated to theoretical Lorenz number L/L_0 as a function of temperature.

4. Conclusion and perspectives

In summary, we have systematically investigated the thermoelectric properties of GNRs with resonant structures using molecular dynamics simulations combined with LSQT methods, explicitly accounting for electron–phonon coupling effects. Our key findings demonstrate that while the introduction of resonant structures moderately reduces both electrical conductivity and Seebeck coefficient, it achieves dramatic suppression of phonon transport, leading to a substantial decrease in phonon thermal conductivity. This phonon suppression effect not only compensates for the degradation in electronic transport properties but ultimately enhances the thermoelectric figure of merit. Through optimized resonant structure design, we achieved a significant improvement in *ZT* from 0.065 in pristine GNRs to approximately 0.135 in resonant structures.

Temperature-dependent studies revealed important deviations from conventional transport behavior in these nanostructures. At lower temperatures, we observed significant violation of the W–F law between σ and κ_{el}, originating from pronounced peaks in the transport distribution function. This decoupling of electronic and thermal transport presents unique opportunities for thermoelectric optimization in nanoscale systems. Our results demonstrate that resonant GNRs offer a promising pathway for enhancing thermoelectric performance through selective phonon suppression while maintaining reasonable electronic transport properties. The ability to tune *ZT* via controlled geometric modifications suggests strong potential for practical applications in thermoelectric energy conversion. These findings provide fundamental insights for designing high-performance graphene-based thermoelectric materials through nanostructure engineering.

Acknowledgments

This project was supported by the National Natural Science Foundation of China (Grant Nos. U22A20210 and

12174276) and the Basic and Applied Basic Research Foundation of Guangdong Province (Grant No. 2024A1515010521).

References

[1] Lee C, Wei X, Kysar J W and Hone J 2008 *Science* **321** 385
[2] Nan H Y, Ni Z H, Wang J, Zafar Z, Shi Z X and Wang Y Y 2013 *J. Raman Spectrosc.* **44** 1018
[3] Geim A and Novoselov K 2007 *Nat. Mater.* **6** 183
[4] Zhang H J, Zheng G G, Chen Y Y, Zou X J and Xu L H 2018 *Chin. Phys. Lett.* **35** 101
[5] Novoselov K S, Geim A K, Morozov S V, Jiang D, Zhang Y and Dubonos S V 2004 *Science* **306** 666
[6] Zhang Y, Tan Y W, Stormer H L and Kim P 2005 *Nature* **438** 201
[7] Lin Y M and Avouris P 2008 *Nano Lett.* **8** 2119
[8] Zhou W X, Cheng Y, Chen K Q, Xie G, Wang T and Zhang G 2020 *Adv. Funct. Mater.* **30** 1903829
[9] Yang G, Yu Q, Geng H and Wang Y 2020 *Sci. China Phys. Mech. Astron.* **63** 217321
[10] Balandin A A, Ghosh S, Bao W, Calizo I, Teweldebrhan D, Miao F and Lau C N 2008 *Nano Lett.* **8** 902
[11] Evans W J, Hu L and Keblinski P 2010 *Appl. Phys. Lett.* **96** 203112
[12] Shiomi J and Maruyama S 2010 *Int. J. Thermophys.* **31** 1945
[13] Guo Z, Zhang D and Gong X G 2009 *Appl. Phys. Lett.* **95** 163103
[14] Xie G, Ju Z, Zhou K, Wei X, Guo Z, Cai Y and Zhang G 2018 *npj Comput. Mater.* **4** 21
[15] Liu Y, Yue J, Liu Y, Nian L L and Hu S 2023 *Chin. Phys. Lett.* **40** 086301
[16] Hu S, Chen J, Yang N and Li B 2017 *Carbon* **116** 139
[17] Jiang J W, Lan J, Wang J S and Li B 2010 *J. Appl. Phys.* **107** 054314
[18] Davis B L and Hussein M I 2014 *Phys. Rev. Lett.* **112** 055505
[19] Xiong S Y, Sääskilahti K, Kosevich Y A, Han H, Donadio D and Volz S 2016 *Phys. Rev. Lett.* **117** 025503
[20] Ma D, Ding H, Meng H, Feng L, Wu Y, Shiomi J and Yang N 2016 *Phys. Rev. B* **94** 165434
[21] Liu H, Li W, Cao Z, Huang X and Ni Y 2023 *Int. J. Heat Mass Transfer* **205** 123903
[22] Huang X, Volz S, Nomura M and Ni Y 2025 *Phys. Rev. B* **111** 174203
[23] Davis B L and Hussein M I 2014 *Phys. Rev. Lett.* **112** 055505
[24] Li W, Zhang W, Huang X, Mu X and Ni Y 2024 *Int. J. Heat Mass Transfer* **220** 124955
[25] Honarvar H and Hussein M I 2018 *Phys. Rev. B* **97** 195413
[26] Wan X, Ma D, Pan D, Yang L and Yang N 2021 *Mater. Today Phys.* **20** 100445
[27] Ma D, Wan X and Yang N 2018 *Phys. Rev. B* **98** 245420
[28] Liu Y Y, Zeng Y J, Jia P Z, Cao X H, Jiang X and Chen K Q 2018 *J. Phys.: Condens. Matter* **30** 275701
[29] Wu C W, Zhou W X, Xie G, Chen X K, Wu D and Fan Z Q 2022 *Nanotechnology* **33** 215402
[30] Jia P Z, Mo Z X, Deng L Q, Zhang Y, Yu X, Zeng Y J, Deng Y X and Xie Z X 2024 *Diam. Relat. Mater.* **141** 110609
[31] Spann B T, Weber J C, Brubaker M D, Harvey T E, Yang L, Honarvar H, Tsai C, Treglia A C, Lee M, Hussein M I and Bertness K A 2023 *Adv. Mater.* **35** 2209779
[32] Zheng Y H, Zeng Y J, Xie G F and Zhou W X 2024 *J. Appl. Phys.* **136** 164301
[33] Wang H, Cheng Y, Fan Z, Guo Y, Zhang Z, Bescond M, Nomura M, Ala-Nissila T, Volz S and Xiong S 2021 *Nanoscale* **13** 10010
[34] Wu X, Cheng Y, Huang S and Xiong S 2024 *Phys. Rev. Appl.* **22** 024038
[35] Wang H, Cheng Y, Nomura M, Volz S, Donadio D, Zhang X and Xiong S 2021 *Phys. Rev. B* **103** 085414
[36] Fan Z, Garcia J H, Cummings A W, Barrios-Vargas J E, Panhans M, Harju A, Ortmann F and Roche S 2021 *Phys. Rep.* **903** 1
[37] Ruffieux P, Wang S, Yang B, Sánchez-Sánchez C, Liu J, Dienel T, Talirz L, Shinde P, Pignedoli C A, Passerone D, Dumslaff T, Feng X, Müllen K and Fasel R 2016 *Nature* **531** 489
[38] Fan Z, Dong H, Harju A and Ala-Nissila T 2019 *Phys. Rev. B* **99** 064308
[39] Chen J, Zhang G and Li B 2010 *Phys. Lett. A* **374** 2392
[40] Wei Z, Yang J, Bi K and Chen Y 2015 *J. Appl. Phys.* **118** 155103
[41] Xiao Y, Liu Y, Tan Z, Zhang B, Xu K, Fan Z, Chen S, Xiong S and Dong H 2025 *Phys. Rev. Mater.* **9** 084603
[42] Azizi F and Rezania H 2025 *Sci. Rep.* **15** 6510
[43] Fan Z, Xiao Y, Wang Y, Ying P, Chen S and Dong H 2024 *J. Phys. Condens. Matter* **36** 245901
[44] Mahan G and Sofo J 1996 *Proc. Natl. Acad. Sci. USA* **93** 7436
[45] Fan Z, Wang H-Q and Zheng J-C 2011 *J. Appl. Phys.* **109** 073713
[46] Zhou J, Yang R, Chen G and Dresselhaus M S 2011 *Phys. Rev. Lett.* **107** 226601
[47] Jeong C, Kim R and Lundstrom M S 2012 *J. Appl. Phys.* **111** 113707
[48] Maassen J 2021 *Phys. Rev. B* **104** 184301
[49] Ding S, Chen X, Xu Y and Duan W 2023 *npj Comput. Mater.* **9** 189
[50] Xu K, Bu H, Pan S, *et al.* 2025 *Mater. Genome Eng. Adv.* e70028
[51] Yue J, Chen R, Ma D and Hu S 2025 *Chin. Phys. Lett.* **42** 036301
[52] Dass D 2018 *Superlattices Microstruct.* **115** 88
[53] Ashcroft N W and Mermin N D 1976 *Solid State Physics* (New York: Holt, Rinehart and Winston) Appendix C 1
[54] Cui L, Guo X, Yu Q, Wei G and Du X 2022 *Int. J. Heat Mass Transf.* **196** 123227
[55] Win T Z, Aung C W, Khandal G and Ghosh S 2025 *Int. J. Mod. Phys. B* 2550182
[56] Mason S, Wesenberg D, Hojem A, Manno M, Leighton C and Zink B 2020 *Phys. Rev. Mater.* **4** 065003